

Quantifying the influence of microstructure on effective conductivity and permeability: virtual materials testing

Matthias Neumann^{a,*}, Ole Stenzel^b, François Willot^c, Lorenz Holzer^b, Volker Schmidt^a

^a*Institute of Stochastics, Ulm University, D-89069 Ulm, Germany*

^b*Institute of Computational Physics, ZHAW Winterthur, CH-8400 Winterthur, Switzerland*

^c*MINES ParisTech, PSL Research University, Centre for Mathematical Morphology, F-77300 Fontainebleau, France*

Abstract

Effective conductivity and permeability of a versatile, graph-based model of random structures are investigated numerically. This model, originally introduced in Gaiselmann et al. (2014) allows one to simulate a wide class of realistic materials. In the present work, an extensive dataset of two-phase microstructures with wide-ranging morphological features is used to assess the relationship between microstructure and effective transport properties, which are computed using Fourier-based methods on digital images. Our main morphological descriptors are phase volume fractions, mean geodesic tortuosity, two “hydraulic radii” for characterizing the length scales of heterogeneities, and a “constrictivity” parameter that describes bottleneck effects. This additional parameter, usually not considered in homogenization theories, is an essential ingredient for predicting transport properties, as observed in Gaiselmann et al. (2014). We modify the formula originally developed in Stenzel et al. (2016) for predicting the effective conductivity and propose a formula for permeability. For the latter one, different geometrical definitions of the hydraulic radius are compared. Our predictions are validated using tomographic image data of fuel cells.

Keywords: Permeability, effective conductivity, constrictivity, mean geodesic tortuosity, predictive simulation, stochastic microstructure modeling.

1. Introduction

It is well-known that the effective properties (e.g. conductivity, permeability) of heterogeneous media, for both, porous or composite materials, strongly depend on microstructural features such as phase volume fraction or tortuosity [1]. Exact results for the effective properties of random structures have been obtained in few cases, most of them related to media with infinitely-many scales (e.g. self-consistent estimates, or the coated-spheres model [2]), which are hardly representative for real microstructures. In functional materials such as solar cells [3], batteries [4] and fuel cells [5], most applications are dealing with microstructures

*Corresponding author. Phone: +49 731 50 23617. Email: matthias.neumann@uni-ulm.de.

characterized by a narrow distribution of typical scales of the heterogeneities which are, due to processing constraints, of similar size. Exact analytical upper and lower bounds [1] correspond to extreme properties and are, in this context, not useful.

Although 3D imaging of materials helps investigating quantitative relationships between
5 microstructure characteristics and transport properties, as done in [6] for the permeability
of sandstone, this approach suffers from the high costs of 3D imaging, and a limited number
of imaged samples. Alternatively, virtual but otherwise realistic microstructures may be
simulated using methods of stochastic geometry [7] and mathematical morphology [8]. We
refer to [9] for a review of the combined use of stochastic modeling and numerical simulations
10 of macroscopic properties, which will be called virtual materials testing in the following.
Efforts have focused, notably, on the Boolean model [10], see e.g. [11, 12], on dilated edge
systems of Laguerre tessellations [13, 14], and, recently, on excursion sets of Gaussian random
fields [15]. Moreover, virtual materials testing has been applied in [16] with respect to
effective conductivity, where a large variety of virtual microstructures is generated by means
15 of a specifically developed stochastic microstructure model. Improvements of the results
obtained in [16] and combinations of virtual materials testing with methods of machine
learning are presented in [17, 18].

In [18], an extensive study making use of 8119 virtual microstructures generated by means
of three different stochastic microstructure models have been conducted. The authors of [18]
20 proposed to use an “intrinsic constrictivity” parameter β that describes bottleneck effects,
in order to discriminate between poorly- and highly-conducting microstructures that exhibit
otherwise similar phase volume fractions ε and similar lengths of transport paths quantified
by mean geodesic tortuosity τ .¹ Note that the definition of constrictivity β is based on
the concept of the so-called continuous phase size distribution [19], strongly related with the
25 granulometry function of mathematical morphology [8], and thus it takes the size distribution
of the transport phase into account. Regarding the importance of the phase size distribution
for effective transport properties, we refer to, e.g., [13, 20].

In [18], an empirical powerlaw formula has been proposed to predict the effective conduc-
tivity (“ M -factor”) as a function of the microstructure characteristics ε, τ and β . The present
30 study builds on the work of Stenzel et al. [18]. First, we show that the powerlaw formula
of [18] systematically underestimates effective conductivity for well conducting microstruc-
tures and propose a refined empirical formula for conductivity that matches numerical data
with much greater accuracy. Second, virtual materials testing is used to systematically in-
vestigate relationships between permeability and the geometrical characteristics ε, τ and β
35 using a database of various virtual microstructures. No length scale relevant to the porous
phase is accounted for in the parameters ε, τ and β whereas permeability is strongly size-
dependent [21]. Therefore, in the rest of the present paper, we make use of an additional
characteristic, namely a geometrical “hydraulic” radius. Based on [22], we discuss two possi-
ble approaches, where the hydraulic radius is defined by means of the specific surface area or
40 by a convex combination of characteristic bottleneck sizes and the median of a “continuous

¹For the definition of constrictivity and mean geodesic tortuosity, we refer to Section 3.

phase size” distribution. The latter approach demonstrates again that the size of bottlenecks is an important microstructure characteristic with respect to permeability [6, 14, 21, 23]. We compare our predictive formulas for permeability with the results obtained in [6]. Furthermore, our formulas are validated based on tomographic image data of real microstructures.

5 The rest of this paper is organized as follows. First, we briefly describe the considered macroscopic properties, i.e. effective conductivity and permeability, and their numerical simulation (Section 2). The definitions of the considered geometric microstructure characteristics are presented in Section 3, with a special emphasis on the hydraulic radius. The simulation of microstructures is recalled in Section 4. A discussion of our results is provided
10 in Section 5. Finally, Section 6 concludes.

2. Effective transport properties and their numerical simulation

2.1. Effective conductivity

Consider a two-phase microstructure with a conducting and insulating phase. Denote by σ_0 the intrinsic conductivity of the former. The M -factor is the normalized effective
15 conductivity, i.e.

$$M = \sigma^{\text{eff}}/\sigma_0. \quad (1)$$

Let J and U denote the current density and the electric potential, respectively. Under steady state conditions, U and J can be determined by solving:

$$\text{div } J = 0, \quad J = -\sigma \nabla U \text{ (conducting phase)}, \quad J = 0 \text{ (insulating phase)}. \quad (2)$$

where σ denotes the local conductivity (see [1], Sections 13.2 and 16.1). A macroscopic gradient of the potential field is applied, as: $\langle \nabla U \rangle_\Omega = (-1, 0, 0)$. Assuming periodic boundary
20 conditions along the frontiers of a domain Ω , the effective conductivity σ^{eff} is determined by

$$\langle J \rangle_\Omega = -\sigma^{\text{eff}} \langle \nabla U \rangle_\Omega, \quad (3)$$

where $\langle \cdot \rangle_\Omega$ denotes an average over the elementary cell Ω . Hereafter we suppose that Ω is large compared to the size of the heterogeneities and, therefore, is representative for the microstructure model. Moreover, we identify the tensor σ^{eff} with its component σ_{11}^{eff} , which
25 is in the following determined by $\sigma_{11}^{\text{eff}} = -\langle J_1 \rangle_\Omega / \langle \partial_1 U \rangle_\Omega$. If not stated otherwise, the software GeoDict [24] is used to compute σ^{eff} for voxelized 3D microstructures of two-phase materials. We recall the formula proposed in [17] for predicting the M -factor:

$$\widehat{M}_1 = \frac{\varepsilon^{1.15} \beta^{0.37}}{\tau^{4.39}}, \quad (4)$$

where $\widehat{M}_1 \approx M$ is an estimate of the normalized effective conductivity. The definitions for β and τ are given below.

2.2. Permeability

We consider viscous flow of incompressible fluids through the pore space of complex microstructures, which is described by Darcy’s law [1, Section 13.5], i.e.

$$\langle v \rangle_{\Omega} = -\frac{\kappa}{\eta} \langle \nabla p \rangle_{\Omega}, \quad (5)$$

where $\langle v \rangle_{\Omega}$, κ , η , $\langle \nabla p \rangle_{\Omega}$ denote the spatial average of the local fluid velocity v , the permeability of the pore space, the dynamic viscosity and the macroscopic pressure gradient with respect to the gradient of the pressure field p , respectively. Note that κ quantifies the influence of microstructure on viscous flow and can be computed from the velocity and pressure fields. These fields, in turn, are obtained by solving the system of differential equations given by

$$\eta \Delta v = \nabla p, \quad \operatorname{div} v = 0, \quad (6)$$

in the pore space, under the constraints that $\langle p \rangle_{\Omega} = 0$ and that v vanishes at the pore-solid interface. The macroscopically applied pressure gradient reads $\langle \nabla p \rangle_{\Omega} = (-1, 0, 0)$. For simulating permeability of voxelized 3D microstructures of porous materials, we use the software GeoDict [24]. We identify the tensorial permeability κ by the component κ_{11} in the following, i.e., we consider the direction of the macroscopic pressure gradient. In contrast to the M -factor, κ (unit: m^{-2}) is not dimensionless.

3. Microstructure characteristics

In order to investigate the influence of microstructure on effective transport properties, we consider the following characteristics: volume fraction ε , mean geodesic tortuosity τ , constrictivity β and hydraulic radius r_{hc} of the transport phase. We emphasize that the volume fraction ε of the transport phase is the volume fraction of the percolating cluster in that phase. We focus on these microstructure characteristics since they allow for the explanation of variations of effective conductivity to a large extent as shown in [16, 17]. A detailed motivation for the choice of the characteristics ε , τ , and β can be found in [16]. Possible modifications in the definition of constrictivity are discussed in [17], where it turned out that the notion of constrictivity considered in [16] is the most meaningful regarding effective conductivity. With respect to permeability, the results of [21] and [25] let us assume that permeability can be appropriately predicted by the same microstructure characteristics as effective conductivity, i.e. by ε , τ , β , and one further microstructure characteristic quantifying the characteristic length scale of the transport phase. The choice of this additional microstructure characteristic is discussed in Section 3.3.

3.1. Mean geodesic tortuosity

The mean geodesic tortuosity τ quantifies the length of paths through the transport phase. To compute τ from 3D image data, we compute all shortest paths beginning at the plane, where transport starts. For this purpose, we use Dijkstra’s algorithm [26] on the voxel grid. Finally, τ is defined as the average over all shortest path lengths divided by the thickness of the material [17].

3.2. Constrictivity

Constrictivity β is a measure for bottleneck effects, which has been introduced for a cylindrical transport phase with periodic constrictions in [27] by $\beta = (r_{\min}/r_{\max})^2$. Here r_{\min} and r_{\max} denote the minimum and maximum radius of the cross-section through the transport phase. A generalization of constrictivity has been introduced in [28], where r_{\min} and r_{\max} are defined for complex microstructures based on two kinds of phase size distributions. To be more precise, r_{\max} is defined as the 50%-quantile of the continuous phase size distribution, while r_{\min} is defined as the 50%-quantile of the MIP-phase size distribution [18] geometrically simulating the mercury intrusion porosimetry [19], where the intrusion is performed in transport direction. Thus, r_{\min} is a direction-dependent characteristic, which can be considered as the radius of the characteristic bottleneck of the transport phase. The values of constrictivity are between 0 and 1 by definition. Values close to 0 indicate strong bottleneck effects, while values close to 1 mean that there are no bottlenecks within the microstructure. For a formal definition of mean geodesic tortuosity and constrictivity in the framework of stationary random closed sets, we refer to [29].

3.3. Hydraulic radius

In the case of viscous flow through tubes with constant cross-section, the hydraulic radius r_{hc} is defined as the ratio of the area of the cross-section and its perimeter [30]. Note that, due to the constant cross-sections, this ratio coincides with the ratio of the volume fraction of the tube and the wetted surface area. For circular cross-sections with radius r_0 , it is $r_{\text{hc}} = r_0/2$. In this case, the permeability κ can be analytically computed [31, Paragraph 17] and we have $\kappa = r_0^2/8 = r_{\text{hc}}^2/2$, i.e., the permeability can be expressed in terms of the hydraulic radius. Since the only limitations of viscous flow in a circular tube arise from friction at the tube walls, the hydraulic radius is considered as a characteristic length scale of the pore space describing the strength of flow limitations caused by friction at the boundary [32, 33]. The concept of the hydraulic radius can be transferred to complex microstructures via $r_{\text{hc,I}} = \varepsilon/S$, see e.g. [34], where S denotes the specific surface area of the pore space, i.e. the mean surface area of the pore-solid interface per unit volume. Note that for the estimation of S from discretized model realizations or tomographic image data, we use the method described in [35]. Alternatively, it was suggested in [21] to define the characteristic length of the pores in the context of viscous flow by means of a quantity describing the characteristic bottleneck of the pore space. Following this idea of [21], in [22] the characteristic length scale of the pores is geometrically defined by $r_{\text{hc,II}} = (r_{\min} + r_{\max})/2$. Moreover, it was shown in [23] that the expression $Mr_{\text{hc,II}}^2/8$ correlates strongly with numerically simulated values of permeability in gas-diffusion layers of polymer electrolyte fuel cells (PEFC). Note that it is not a priori clear, why $r_{\text{hc,II}}$ is defined as the average of r_{\min} and r_{\max} . In Section 5.2 we define $r_{\text{hc,II}}$ as the convex combination

$$r_{\text{hc,II}} = ar_{\min} + (1 - a)r_{\max}, \quad (7)$$

where $0 < a < 1$ is optimized such that $r_{\text{hc,II}}$ is meaningful regarding permeability. Analogously, we introduce a scaling factor $b > 0$ in the definition of $r_{\text{hc,I}}$, i.e.,

$$r_{\text{hc,I}} = b\varepsilon/S. \quad (8)$$

The optimization of the parameters a and b is performed on the basis of virtual microstructures generated by stochastic modeling.

4. Generation of virtual microstructures

For the generation of virtual microstructures, we use the stochastic graph-based model introduced in [16]. This model is able to simulate virtual microstructures for a wide range of microstructure characteristics ε, τ and β . The idea of the model is as follows. To begin with, a random geometric graph model is used to define a completely connected network, which is then locally dilated, i.e., the edges of the network are dilated by random dilation radii. The intensity of vertices in the network, the anisotropy of the orientation of edges as well as the mean and the variance of the random dilation radii can be adjusted by the aid of model parameters. This means, in turn, that the microstructure characteristics ε depending on the mean dilation radius, τ depending on the anisotropy of edges, and β depending on the variance of the dilation radii can be controlled by the model parameters [16]. Thus, we use the dilated network as the transport phase in the following. Note that, depending on whether we are interested in effective conductivity or in permeability, the transport phase is either the conductive phase or the phase, in which the fluid flows.

Three virtual microstructures generated by the stochastic graph-based model described above for different values of model parameters are visualized in Figure 1. One can observe that the constrictivity can be varied strongly in the model. In the microstructure depicted in Figure 1 (c), the transport phase consists of large regions which are connected by very thin channels. Thus many narrow constriction appear resulting in the small value of $\beta = 0.01$.

To derive quantitative relationships between microstructure characteristics and effective transport properties, we consider virtual microstructures generated by the stochastic graph-based model described above. Note that in a previous study, 8119 virtual microstructures have been simulated to investigate the influence of microstructure on effective conductivity [18]. In the present paper we use the 8119 microstructures when investigating effective conductivity and restrict ourselves to a selection of 66 virtual microstructures in the case of flow since the numerical simulations of permeability are more time-consuming than the ones of effective conductivity. This means that the prediction formulas for effective conductivity are more reliable, since they are obtained on the basis of a larger data set. Nevertheless, the quantitative relationships derived for permeability also admit appropriate predictions for real microstructures the morphology of which differs from the 66 selected virtual microstructures, see Figure 8 and Section 5.2.

The microstructure characteristics $\varepsilon, S, r_{\max}, r_{\min}, \beta, \tau$ of the selected 66 virtual microstructures are shown in Figure 2. On the one hand, S and β can be varied independently of ε , i.e., there exist microstructures having a large value of both, ε and β . For these microstructures, Equation (4) leads to an underestimation of M , which is discussed in detail in Section 5.1. On the other hand, τ, r_{\max} and r_{\min} can not be varied independently of ε . It is not surprising that for increasing ε the values of r_{\max} and r_{\min} increase. Furthermore, with decreasing volume fraction the length of transport paths through the material typically increases and thus

τ increases for decreasing values of ε . For a visualization of the microstructure characteristics of all 8119 virtual microstructures, we refer to Figure 5 in [18].

5. Results and discussion

In this section, we present and discuss our results regarding quantitative microstructure-property relationships for effective conductivity (Section 5.1) and permeability (Section 5.2). Finally, a summary of the main results is given (Section 5.3).

5.1. Prediction of effective conductivity using geometrical microstructure characteristics

Based on virtual microstructures, generated with the same model as described in Section 4, Equation (4) has been proposed in [17] to estimate the M -factor. In particular, in [17], it has also been shown that Equation (4) is appropriate to predict the M -factor of microstructures in solid-oxide fuel cell (SOFC) anodes and ceramic diaphragms which have been reconstructed by tomographic 3D imaging. For these materials, effective conductivity has been determined with numerical simulation and also with experimental characterization (from electrical four-point-measurements). The predictions by Equation (4) match well with experimental results from the same materials. Note that for such microstructures the numerical values of M are less than 0.2. The goodness-of-fit of Equation (4) for the 8119 virtual microstructures, which is visualized in Figure 3, reveals the following. On the one hand, a mean absolute percentage error (MAPE) of 13.6 % and a coefficient of determination $R^2 = 0.984$ have been computed. This can be considered as a good fit, taking into consideration that the M -factor of many different microstructures is approximated by only three aggregated microstructure characteristics. For comparison, the best prediction of M by ε, τ and β obtained by random forests (RF) leads to a MAPE of 8.5 % and $R^2 = 0.999$ [18]. On the other hand, as shown in Figures 3a and 3c, Equation (4) tends to underestimate effective conductivity for large M -factors. This effect has also been observed when using Equation (4) to predict effective diffusivity² in the pore space of silica monoliths based on tomographic image data [36]. In the following, we investigate the behavior of Equation (4) in the dilute limit, i.e. in the case when the non-conductive phase vanishes, and compare it to theoretical results.

In the dilute limit $\varepsilon \rightarrow 1$, we expect the following asymptotic expansion for the M -factor [1, Section 19.1]:

$$M = 1 - c(1 - \varepsilon) + \mathcal{O}((1 - \varepsilon)^2), \quad (9)$$

where $c > 0$ is a constant depending on the shape of the obstacles. This behavior is clearly not recovered by Equation (4) if, for instance, the constrictivity β does not tend to 1 in the dilute limit. Consider, e.g., conduction in the three-dimensional space with non-conductive spherical inclusions located on the cubic grid $\delta\mathbb{Z}^3$, where $\delta > 0$ and \mathbb{Z} denotes the set

²Fickian diffusion in porous silica monoliths is considered in [36]. Fickian diffusion is mathematically analogous to electric conduction. Thus prediction formulas for the M -factor can be used to predict effective diffusivity.

of integers. Formally, the conducting phase is then given by $\Xi = \mathbb{R}^3 \setminus (\delta\mathbb{Z}^3 \oplus B(o, \rho))$, where $B(o, \rho)$ denotes the sphere centered at the origin with radius $\rho > 0$ and \oplus denotes Minkowski addition [7]. If the radius ρ of the spherical inclusions tends to zero, we obtain $\lim_{\rho \rightarrow 0} r_{\min} = \delta/\sqrt{2}$ and $\lim_{\rho \rightarrow 0} r_{\max} = \delta\sqrt{3}/2$. Since r_{\min} is the maximum radius r such that 50% of the conducting phase can be filled by spheres of radius r , r_{\min} is the radius of the largest sphere which can go through a bottleneck between four grid points forming a square (see Figure 4a). This radius is $\delta/\sqrt{2}$ if ρ tends to 0. The radius r_{\max} is the maximum radius such that the conducting phase can be covered by spheres of radius r_{\max} , which are completely contained in the conducting phase. The complete conducting phase can be covered by the union of spheres centered at the translated grid $\delta(\mathbb{Z}+1/2)^3$ with radius $\delta\sqrt{3}/2$, which is illustrated in Figure 4b. Since the maximum distance from an arbitrary point in the three-dimensional space to a grid point of $\delta\mathbb{Z}^3$ is $\delta\sqrt{3}/2$, we have $\lim_{\rho \rightarrow 0} r_{\max} = \delta\sqrt{3}/2$. Consequently, $\lim_{\rho \rightarrow 0} \beta = 2/3$, which is the limiting value of the constrictivity when $\delta \rightarrow \infty$ ($\varepsilon \rightarrow 1$). Thus, estimate (4) is too sensitive on the constrictivity in the dilute regime. As a result, \widehat{M}_1 underestimates M when M is large.

We modify formula (4) accordingly, where we keep the dependency on ε and τ as power-laws, but let the exponent vary slowly with constrictivity:

$$\widehat{M}_2 = \frac{\varepsilon^{1.67-0.48\beta}}{\tau^{5.18}}. \quad (10)$$

This formula is obtained by assuming that $M = \varepsilon^{\alpha_1 + \alpha_2\beta} \tau^{\alpha_3}$ for some parameters $\alpha_1, \alpha_2, \alpha_3 \in \mathbb{R}$ and fitting these parameters by linear regression to the numerically computed M -factors of the 8119 virtual microstructures. Note that Equation (10) fulfills the theoretical requirement that \widehat{M}_2 tends to 1 in the dilute limit, since ε and τ tend to 1 in this case. For structures approaching the dilute limit under the additional conditions that (i) $\lim_{\varepsilon \rightarrow 1} \tau/\varepsilon^{-\gamma} = 1$ for some $0 < \gamma < 1.19/5.18 \approx 0.23$, (ii) the limit β^* of β exists in the dilute limit and (iii) the derivative of β with respect to ε exists and is bounded, the prediction \widehat{M}_2 in Equation (10) behaves as M in Equation (9). In this case one can show that the constant c in Equation (9) is given by $c = 1.67 - 5.18\gamma - 0.48\beta^* > 0$. In order to get a better understanding of Condition (i), the relationship between τ and ε is visualized in Figure 6b for large volume fractions, together with the curve $\tau = \varepsilon^{0.23}$.

The predictions obtained by applying Equation (10) on the 8119 virtual microstructures are visualized in Figure 3b and d. Note that using Equation (10), the M -factor is not underestimated, nor overestimated on average, when $M > 0.4$. But, the M -factor is slightly overestimated whenever $0.05 < M < 0.4$. Note that for M between 0 and 0.2, the M -factor is also overestimated by \widehat{M}_1 , see Figure 3c. The MAPE of \widehat{M}_2 is about 18.28%, which is significantly larger than the MAPE of \widehat{M}_1 . However, this can be attributed to large errors for low values of M . If we only consider structures, where the M -factor is larger than 0.05, then the MAPE of \widehat{M}_2 is 10.14% which is more accurate than the MAPE of \widehat{M}_1 , which is 10.33% in that case. The higher the value of M , the better the prediction of \widehat{M}_2 . Moreover, Figure 3c suggests that the prediction by \widehat{M}_1 is biased not only for simulated M -factors close to 1. Due to these results and the fact that \widehat{M}_2 converges to 1 in the dilute limit, the

prediction by Equation (10), i.e. by \widehat{M}_2 , is more reliable and more accurate in the most cases and thus a refinement of the prediction by \widehat{M}_1 given in Equation (4).

A further interesting result regarding Equation (10) is obtained when having a closer look on those structures for which the relative prediction error is below 1%, see Figure 5. One can observe that for those structures the upper bound of M corresponds well to the theoretical bound for the M -factor in the Boolean model with spherical grains, i.e.

$$M \leq \frac{2z\varepsilon}{1 - \varepsilon + 2z} \quad (11)$$

where $z \approx 0.56$, see [37, 38]. Note that this bound is obtained using a general third-order bound [1, Equation (21.34)] for effective conductivity, which depends on the three-point coverage probability function of the conducting phase. This observation suggests that Equation (10) leads to good predictions for microstructures exhibiting common features with realizations of the Boolean model with spherical grains in terms of the three-point coverage probability function.

We now use Equation (10) to estimate effective conductivity for tomographic image data of real microstructures. We consider electric and ionic conduction in microstructures consisting of nickel and yttrium-stabilized zirconia (YSZ), which are used as anode material in SOFC. The microstructures are investigated based on image data obtained by FIB-SEM tomography. For detailed information regarding these microstructures, we refer to [18, 39], where these microstructures have also been considered for the validation of Equation (4). Furthermore, we compare geometrically predicted M -factors with numerically simulated ones of the solid phase of microstructures appearing in gas-diffusion layers of PEFC. Note that 3D imaging of these microstructures is performed by X-ray synchrotron tomography where they have been analyzed with respect to ε , τ and β in [25]. The results of the validation are visualized in Figure 6. Except of two outliers for the SOFC microstructures, both, Equations (4) and (10), are appropriate to predict the M -factor of SOFC microstructures. While \widehat{M}_1 leads to a MAPE of 19.5 % for the considered real microstructures and overestimates M for the PEFC microstructures, which exhibit relatively high volume fractions of the transport phase, the prediction by \widehat{M}_2 is better with a MAPE of 16.2 %. In particular, no trend of over- or underestimation can be observed for the prediction by \widehat{M}_2 . Thus, the refinement of predicting M by \widehat{M}_2 instead of \widehat{M}_1 is also reflected when considering real microstructures used in fuel cells.

Additionally, we simulate the effective conductivity for three virtual structures, where the transport phase is either given by a system of spheres itself or by its complement. In particular, the morphology of these structures completely differs from the structures, given by randomly dilated graphs, which have been used to empirically derive Equations (4) and (10) and which are described in Section 4. For these three structures, we choose microstructures which lead to a high M -factor despite of a relatively low volume fraction and vice versa. The first microstructure is given by a system of non-overlapping, equally sized spheres, where the complement of the spheres ($\varepsilon = 0.66$) is considered as the conducting phase. Such a structure, defined as the complement of a sphere packing, can be considered as a foam-like structure, which is well-connected and has a large M -factor. The remaining two

microstructures are designed to yield a low effective conductivity, i.e., the structures consist of systems of slightly overlapping spheres with constant diameter $d > 0$, where the union of spheres is considered as the conducting phase. The midpoints are distributed completely at random under the condition that the distance between midpoints of spheres is larger than $0.86d$ and $0.9d$ for the second and third structure ($\varepsilon = 0.51, \varepsilon = 0.44$), respectively. The intensity of spheres is chosen such that we get volume fractions of $\varepsilon = 0.51$ and $\varepsilon = 0.44$, respectively. Note that strong bottleneck effects occur in these two structures. Effective conductivity of these structures is simulated as described in [40]. The results are included in Figure 6 b. The estimation of effective conductivity by Equation (10) leads to relative errors of 7 %, 66 % and 100 %, respectively. The corresponding relative errors regarding Equation (4) are significantly smaller (9 %, 19 % and 27 %). These results show that the more the microstructures deviate from the ones in Section 4, the higher are the errors when relating the M -factor to ε, τ and β by Equation (10) and Equation (4). Note that this effect is less pronounced when using Equation (4) in the case of low M -factors.

5.2. Prediction of permeability by geometrical microstructure characteristics

Based on 66 virtual microstructures, which are generated as described in Section 4, a prediction formula for effective permeability κ is derived by regression analysis. We follow [21] and [23], and consider the approximation $\hat{\kappa}$ for κ given by

$$\hat{\kappa} = \frac{r_{\text{hc}}^2}{8} M. \quad (12)$$

Provided that geometrical prediction formulas for M are available, prediction of κ means that r_{hc} has also to be predicted by suitable microstructure characteristics. In the following, we empirically derive prediction formulas for r_{hc} of the types $r_{\text{hc,I}}$ and $r_{\text{hc,II}}$ introduced in Section 3.3, i.e., we fit the parameters a and b appearing in Equations (7) and (8) on the basis of the 66 virtual microstructures. For the prediction of M , we consider Equations (4) and (10), as well as the neural network (NN) and the RF trained with the 8119 virtual microstructures and provided as supplementary material in [18]. In a further step we re-fitted the parameters of Equations (4) and (10) in order to improve the fit with respect to permeability. To be more precise, M in Equation (12) is assumed to take either the form $M = \varepsilon^{\theta_1} \beta^{\theta_2} \tau^{\theta_3}$ or $M = \varepsilon^{\alpha_1 + \alpha_2 \beta} \tau^{\alpha_3}$, where $\theta_i, \alpha_i \in \mathbb{R}$ for $i = 1, 2, 3$ are parameters which are fitted, in order to obtain the best fit for κ . Table 1 shows the result of our fitting procedure for the different model types, denoted by I.A, ..., I.F, II.A, ..., II.F. The fitted parameters as well as the goodness-of-fit in terms of the mean-squared error (MSE) on the log-scale and the MAPE are given. The goodness-of-fit for the model types I.B, I.E, II.E, II.F is visualized in Figure 7.

Figure 7 shows that the relationship between microstructure characteristics and permeability is well reflected by all proposed models, even if we use the model type I.B, i.e., the model type with the worst fit among all considered model types. One can also observe that the other model types shown in Figure 7 (I.E, II.E, II.F) are in particular better than model type I.B for microstructures, where κ is between $10^{-15} m^{-2}$ and $10^{-12} m^{-2}$.

Table 1: Results of fitting the different prediction models to the numerically simulated permeabilities of 66 virtual microstructures. Recall that $r_{\text{hc,I}} = b\varepsilon/S$, $r_{\text{hc,II}} = ar_{\text{min}} + (1 - a)r_{\text{max}}$, see Equations (8) and (7), respectively. The fitted parameters and errors are given.

model type			fitted parameters		goodness-of-fit	
name	r_{hc}	M	a, b (resp.)	α, θ (resp.)	MSE (log-scale)	MAPE
I.A	$r_{\text{hc,I}}$	$\varepsilon^{1.15}\beta^{0.37}\tau^{-4.39}$	1.33		0.35	56.35 %
I.B	$r_{\text{hc,I}}$	$\varepsilon^{1.67-0.48\beta}\tau^{-5.18}$	1.37		0.43	65.32 %
I.C	$r_{\text{hc,I}}$	NN	1.25		0.30	50.65 %
I.D	$r_{\text{hc,I}}$	RF	1.26		0.29	49.61 %
I.E	$r_{\text{hc,I}}$	$\varepsilon^{\theta_1}\beta^{\theta_2}\tau^{\theta_3}$	2.08	(3.56, 0.78, -1.67)	0.18	34.50 %
I.F	$r_{\text{hc,I}}$	$\varepsilon^{\alpha_1-\alpha_2\beta}\tau^{\alpha_3}$	1.37	(2.71, -2.29, -3.05)	0.21	38.50 %
II.A	$r_{\text{hc,II}}$	$\varepsilon^{1.15}\beta^{0.37}\tau^{-4.39}$	0.80		0.28	47.57 %
II.B	$r_{\text{hc,II}}$	$\varepsilon^{1.67-0.48\beta}\tau^{-5.18}$	0.82		0.32	43.82 %
II.C	$r_{\text{hc,II}}$	NN	0.86		0.17	32.29 %
II.D	$r_{\text{hc,II}}$	RF	0.86		0.16	31.06 %
II.E	$r_{\text{hc,II}}$	$\varepsilon^{\theta_1}\beta^{\theta_2}\tau^{\theta_3}$	0.94	(2.14, -0.05, -2.44)	0.17	34.54 %
II.F	$r_{\text{hc,II}}$	$\varepsilon^{\alpha_1-\alpha_2\beta}\tau^{\alpha_3}$	0.85	(2.08, 0.13, -2.49)	0.21	39.56 %

Results are listed in Table 1. First, comparing the pairs of model types I.A-I.F, for which M is predicted in the same way, the model type using $r_{\text{hc,II}}$ instead of $r_{\text{hc,I}}$ leads to better results. Accordingly, using r_{min} and r_{max} to determine a geometrical hydraulic radius leads to more accurate predictions with respect to permeability than the use of the specific surface area S and the volume fraction ε . Note that the fitted values of the parameters a and b are similar for the model types I.A,...,I.F and II.A,...,II.F. The parameters a and b are only clearly different for the model types I.E and II.E. The fitted value of b is larger than 1 for all model types, i.e., in order to predict κ appropriately using $r_{\text{hc,I}}$ the term ε/S has to be scaled by a factor larger than 1. For the model types II.A-II.F, the fitted value of a is larger than 0.8. It can therefore be concluded that r_{min} is the dominating part, when the hydraulic radius for complex microstructures is defined by a convex combination of r_{min} and r_{max} . In other words, the radius of the characteristic bottleneck is an important quantity with respect to permeability. This result is in good accordance with previous studies investigating the relationship between microstructure and permeability based on experiments and simulations [6, 21]. Different formulas relating microstructure with permeability of sandstone are discussed in [6], where one of the formulas leading to a good approximation $\hat{\kappa}$ of κ regarding the MSE on the log-scale is

$$\hat{\kappa} = \vartheta r_c^2 M. \quad (13)$$

Here r_c denotes the radius of the characteristic bottleneck and $\vartheta = 0.03$ is a fitted parameter. Note that Equation (13) coincides with Equation (12) if the hydraulic radius is defined via $r_{\text{hc}} = r_c$ and if $\vartheta = 1/8$. Equation (13) is empirically derived based on the pore space of

real microstructures, for which M can be well approximated via a modified Archie's law $M = 2.31\varepsilon^{2.29}$. The definition of r_c is similar to the one of r_{\min} . To be precise, r_c is defined as the maximum radius such that a sphere can pass through the transport phase. If we substitute r_c by r_{\min} and M by \widehat{M}_2 , which is a function of ε, τ and β , then we obtain $\vartheta = 0.126$ by fitting the parameter ϑ in Equation (13) to the 66 virtual microstructures considered in the present paper. For the corresponding MSE on the log-scale and MAPE, the values of 0.77 and 36.38 % are obtained, respectively. Note that the MSE on the \log_{10} -scale for the structures in [6] is 0.062, which is equivalent to a MSE on the log-scale of 0.33. The best prediction formula obtained in [6] is given by

$$\widehat{\kappa} = 0.094 \varepsilon^{0.81} r_c^2 M^{1.88} \quad (14)$$

leads to a MSE on the log-scale of 0.24 for the sandstone structures, which is only slightly worse than the best prediction formulas in the present paper. Nevertheless, by the stochastic graph-based model, see Section 4, we generate virtual microstructures for a large range of different characteristics. In particular, the M -factor of these structures can not be predicted via a modified Archie's law as $M = 2.31\varepsilon^{2.29}$ [16]. From this point of view we claim that our prediction formulas are more universal than the ones empirically derived in [6]. Moreover, when substituting r_c by r_{\min} , M by either \widehat{M}_1 or \widehat{M}_2 , and fitting the numerical values in Equation (14) to the 66 virtual microstructures described in Section 4, we are nearly in the same situation of model type II.E and II.F, compare Table 1.

Furthermore, the best fit of permeability is obtained by model type II.D. Recall that in model type II.D, we predict M in Equation (12) by the RF trained in [18] without any modification. The model types I.E and II.E are only negligibly worse. On the one hand, it turned out that a refitting of the parameters α and θ is necessary to significantly increase the goodness-of-fit compared to predicting M by either Equation (4) or Equation (10). On the other hand, such parametric results have the advantage that they are better interpretable than the prediction formulas obtained by methods of machine learning (I.C, I.D, II.C, II.D). Note that the best parametric prediction formulas for κ are obtained by model type I.E leading to

$$\widehat{\kappa} = 0.54 \frac{\varepsilon^{5.56} \beta^{0.78}}{S^2 \tau^{1.67}} \quad (15)$$

and model type II.E resulting in

$$\widehat{\kappa} = \frac{(0.94 r_{\min} + 0.06 r_{\max})^2}{\beta^{0.05}} \frac{\varepsilon^{2.14}}{8 \tau^{2.44}}. \quad (16)$$

Equation (15) does not depend on the specific values of r_{\min} and r_{\max} . The effect of bottlenecks is represented only in terms of the dimensionless characteristics β . The length scale is captured by the specific surface area, the unit of which is m^{-1} . In Equation (16), the length scale is taken into account by r_{\min} and r_{\max} , while the specific surface area does not appear. It is counterintuitive that $\beta^{0.05}$ appears in the denominator of Equation (16) since $\widehat{\kappa}$ increases with smaller values of constrictivity. An optimization of parameters for model type II.E with the constraint $\theta_2 > 0$ gives $a = 0.94$ and $\theta = (2.12, 0, 2.46)$ leading to nearly

the same errors. The same effect occurs for model type II.F. Under the constraint $\alpha_2 < 0$, we obtain $\alpha_2 = 0$, i.e., model types II.E and II.F coincide and Equation (16) changes to

$$\hat{\kappa} = (0.94 r_{\min} + 0.06 r_{\max})^2 \frac{\varepsilon^{2.14}}{8 \tau^{2.44}}. \quad (17)$$

Note that the equations resulting from model types I.E and II.E reflect the importance of narrow bottlenecks for permeability, which is in good accordance with the results obtained in [6, 21, 23, 14].

The prediction formulas are validated by considering tomographic image data of five sponge-like structures, where flow in the pore space is simulated in all three main directions. In doing so, we obtain 15 values of permeability which we relate to the corresponding microstructure characteristics. The porosities, i.e. the volume fractions of the transport phase, of the structures range from 0.66 to 0.86. In these sponge-like structures, bottlenecks occur due to small holes in the pore walls, which connect much larger cellular pore bodies. Therefore, r_{\max} is much larger than r_{\min} and thus the values of β are all below 0.05.

Figure 8 shows a comparison between the geometrically predicted and numerically simulated values of permeability. Here one can observe that model type II.D and Equation (17) obtained by model types II.E and II.F lead to a relatively good prediction for κ , while model type I.E underestimates κ for each of the considered microstructures. Here we want to emphasize that the sponge-like structures considered for validation exhibit a different morphology than the virtual microstructures for which parameter fitting is performed. Moreover, for some of the sponge-like structures, the values of κ are larger than the maximum value of κ simulated for the selected virtual microstructures, see Figure 7. Thus, the good accordance between permeabilities predicted by model type II.D and Equation (17) shows their predictive power.

5.3. Summary of main results

The main results regarding the prediction of effective conductivity in terms of the M -factor and the prediction of permeability are given. For convenience of the reader, the proposed formulas are summarized in Table 2. To predict the M -factor, Equation (4) of [17] is modified resulting in Equation (10), which is – in contrary to the previous prediction formula – consistent with theoretical results in the dilute limit, i.e., in the case that the non-conductive phase vanishes. Equation (10) leads to a better prediction of M except for the case in which $M < 0.05$. Since $M \leq \varepsilon$, see [1], we particularly recommend to use Equation (4) if $\varepsilon < 0.05$. For permeability two parametric prediction formulas are obtained in Equations (15) and (17), which lead to a nearly identical goodness-of-fit, see Table 1. While Equation (15) predicts κ by means of ε, β, τ and S , Equation (17) uses $\varepsilon, r_{\min}, r_{\max}$ and τ . This means that instead of the surface area S , detailed information of r_{\min} and r_{\max} is taken into account in Equation (17). In Equation (15), the values r_{\min} and r_{\max} appear in an aggregated form as $\beta = r_{\min}^2 / r_{\max}^2$. Finally, note that all these formulas are empirically derived based on extensive simulations of the microstructure model described in Section 4. Limitations of the prediction formulas for microstructures exhibiting a completely different morphology are discussed at the end of Section 5.1 with respect to effective conductivity.

Table 2: Overview of formulas for the prediction of M -factor and permeability.

effective property	reference number	prediction formula
M -factor	Equation (4)	$\widehat{M} = \varepsilon^{1.15} \beta^{0.37} \tau^{-4.39}$
M -factor	Equation (10)	$\widehat{M} = \varepsilon^{1.67-0.48\beta} \tau^{-5.18}$
permeability	Equation (15)	$\widehat{\kappa} = 0.54 \varepsilon^{5.56} \beta^{0.78} S^{-2} \tau^{-1.67}$
permeability	Equation (17)	$\widehat{\kappa} = (0.94 r_{\min} + 0.06 r_{\max})^2 \varepsilon^{2.14} \tau^{-2.44} / 8$

6. Conclusions

In the present paper, we investigate microstructure-property relationships with respect to effective conductivity and permeability by virtual materials testing, i.e., we propose geometrical prediction formulas for these transport properties. Regarding effective conductivity, we refine a prediction formula proposed in [17], which quantifies the relationship between the M -factor, i.e. the ratio of effective and intrinsic conductivity, and the microstructure characteristics volume fraction, mean geodesic tortuosity and constrictivity. In contrast with previous works, the new formula is able to capture the behavior of effective conductivity in the dilute limit, i.e. in the case when the non-conducting phase vanishes. Our formula also leads to a better prediction for the virtual microstructures outside of the percolating limit for the conducting phase, i.e., as long as the M -factor is larger than 0.05. Moreover, our prediction formula has been validated on tomographic image data of real microstructures, where we obtain a mean absolute percentage error of 16.2%. Limitations of the refined prediction formula are discussed at the example of virtual structures, the morphology of which differs strongly from the ones which have been used for fitting the formula.

Furthermore, we also address permeability and investigate several prediction formulas, based on two geometrical definitions of the hydraulic radius entering the formulas. Numerical results show that the prediction formulas give accurate estimates when the M -factor is predicted by volume fraction, mean geodesic tortuosity and constrictivity using the random forest method trained in [18] and defining the hydraulic radius by means of the radius of the characteristic bottleneck. Moreover, parametric prediction formulas with a comparable accuracy are obtained, when the proportionality between permeability and the M -factor is loosened. These parametric prediction formulas have the advantage that they allow for a better interpretability. It is also shown that the proposed prediction formulas are able to predict permeability for real microstructures observed in tomographic image data. Overall, our results reveal that the characteristic bottleneck of a microstructure strongly influences its permeability.

References

- [1] S. Torquato. Random Heterogeneous Materials: Microstructure and Macroscopic Properties. Springer, New York, 2002.

- [2] Z. Hashin. The elastic moduli of heterogeneous materials. Journal of Applied Mechanics, 29(1):143–150, 1962.
- [3] D.W. DeQuilettes, S. M. Vorpahl, S. D. Stranks, H. Nagaoka, G. E. Eperon, M. E. Ziffer, H. J. Snaith, and D. S. Ginger. Impact of microstructure on local carrier lifetime in perovskite solar cells. Science, 348:683–686, 2015.
- [4] J. R. Wilson, J. S. Cronin, S. A. Barnett, and S. J. Harris. Measurement of three-dimensional microstructure in a LiCoO_2 positive electrode. Journal of Power Sources, 196(7):3443–3447, 2011.
- [5] B. S. Prakash, S. S. Kumar, and S. T. Aruna. Properties and development of Ni/YSZ as an anode material in solid oxide fuel cell: A review. Renewable and Sustainable Energy Reviews, 36:149–179, 2014.
- [6] C. H. Arns, M. A. Knackstedt, and N. S. Martys. Cross-property correlations and permeability estimation in sandstone. Physical Review E, 72(4):046304, 2005.
- [7] S. N. Chiu, D. Stoyan, W. S. Kendall, and J. Mecke. Stochastic Geometry and its Applications. J. Wiley & Sons, Chichester, 3rd edition, 2013.
- [8] G. Matheron. Random Sets and Integral Geometry. J. Wiley & Sons, New York, 1975.
- [9] D. Jeulin. Morphology and effective properties of multi-scale random sets: A review. Comptes Rendus Mécanique, 340(4):219 – 229, 2012.
- [10] J. Serra. The Boolean model and random sets. Computer Graphics and Image Processing, 12:99–126, 1980.
- [11] C. Scholz, F. Wirner, M. A. Klatt, D. Hirneise, G. E. Schröder-Turk, K. Mecke, and C. Bechinger. Direct relations between morphology and transport in Boolean models. Physical Review E, 92(4):043023, 2015.
- [12] T. Prill, D. Jeulin, F. Willot, J. Balach, and F. Soldera. Prediction of effective properties of porous carbon electrodes from a parametric 3D random morphological model. Transport in Porous Media, 120(1):141–165, 2017.
- [13] J. Skibinski, K. Cwieka, T. Kowalkowski, B. Wysocki, T. Wejrzanowski, and K. J. Kurzydłowski. The influence of pore size variation on the pressure drop in open-cell foams. Materials & Design, 87:650–655, 2015.
- [14] D. Westhoff, J. Skibinski, O. Šedivý, B. Wysocki, T. Wejrzanowski, and V. Schmidt. Investigation of the relationship between morphology and permeability for open-cell foams using virtual materials testing. Materials & Design, 147:1–10, 2018.
- [15] S. Barman, H. Rootzén, and D. Bolin. Prediction of diffusive transport through polymer films from characteristics of the pore geometry. AIChE Journal, 65(1):446–457, 2019.

- [16] G. Gaiselmann, M. Neumann, O. M. Pecho, T. Hocker, V. Schmidt, and L. Holzer. Quantitative relationships between microstructure and effective transport properties based on virtual materials testing. AICHE Journal, 60(6):1983–1999, 2014.
- [17] O. Stenzel, O. M. Pecho, L. Holzer, M. Neumann, and V. Schmidt. Predicting effective conductivities based on geometric microstructure characteristics. AICHE Journal, 62:1834–1843, 2016.
- [18] O. Stenzel, M. Neumann, O. M. Pecho, L. Holzer, and V. Schmidt. Big data for microstructure-property relationships: A case study of predicting effective conductivities. AICHE Journal, 63(9):4224–4232, 2017.
- [19] B. Münch and L. Holzer. Contradicting geometrical concepts in pore size analysis attained with electron microscopy and mercury intrusion. Journal of the American Ceramic Society, 91:4059–4067, 2008.
- [20] S. Torquato and M. Avellaneda. Diffusion and reaction in heterogeneous media: pore size distribution, relaxation times, and mean survival time. The Journal of Chemical Physics, 95(9):6477–6489, 1991.
- [21] A. J. Katz and A. H. Thompson. Quantitative prediction of permeability in porous rock. Physical Review B, 34:8179–8181, 1986.
- [22] L. Holzer, O. Stenzel, O. M. Pecho, T. Ott, G. Boiger, M. Gorbar, Y. De Hazan, D. Penner, I. Schneider, R. Cervera, and P. Gasser. Fundamental relationships between 3D pore topology, electrolyte conduction and flow properties: Towards knowledge-based design of ceramic diaphragms for sensor applications. Materials & Design, 99:314–327, 2016.
- [23] L. Holzer, O. Pecho, J. Schumacher, P. Marmet, F. N. Büchi, A. Lamibrac, and B. Münch. Microstructure-property relationships in a gas diffusion layer (GDL) for polymer electrolyte fuel cells, part II: pressure-induced water injection and liquid permeability. Electrochimica Acta, 241:414–432, 2017.
- [24] GeoDict. www.geodict.com, 2017.
- [25] L. Holzer, O. Pecho, J. Schumacher, P. Marmet, O. Stenzel, F. N. Büchi, A. Lamibrac, and B. Münch. Microstructure-property relationships in a gas diffusion layer (GDL) for polymer electrolyte fuel cells, part I: Effect of compression and anisotropy of dry GDL. Electrochimica Acta, 227:419–434, 2017.
- [26] K. Thulasiraman and M. N. S. Swamy. Graphs: Theory and Algorithms. J. Wiley & Sons, New York, 1992.
- [27] E. E. Petersen. Diffusion in a pore of varying cross section. AICHE Journal, 4(3):343–345, 1958.

- [28] L. Holzer, D. Wiedenmann, B. Münch, L. Keller, M. Prestat, P. Gasser, I. Robertson, and B. Grobóty. The influence of constrictivity on the effective transport properties of porous layers in electrolysis and fuel cells. Journal of Materials Science, 48:2934–2952, 2013.
- 5 [29] M. Neumann, C. Hirsch, J. Staněk, V. Beneš, and V. Schmidt. Estimation of geodesic tortuosity and constrictivity in stationary random closed sets. Scandinavian Journal of Statistics, in print, 2019. <https://doi.org/10.1111/sjos.12375>.
- [30] F. M. White. Viscous Fluid Flow. McGraw-Hill, New York, 3rd edition, 2006.
- [31] L. D. Landau and E. M. Lifshitz. Course of Theoretical Physics. Volume 6: Fluid
10 Mechanics. Pergamon Press, Oxford, 2nd edition, 1987.
- [32] J. B. Walsh and W. F. Brace. The effect of pressure on porosity and the transport properties of rock. Journal of Geophysical Research: Solid Earth, 89(B11):9425–9431, 1984.
- [33] P. Wong, J. Koplik, and J. P. Tomanic. Conductivity and permeability of rocks. Physical
15 Review B, 30(11):6606, 1984.
- [34] M. N. Panda and L. W. Lake. Estimation of single-phase permeability from parameters of particle-size distribution. American Association of Petroleum Geologists Bulletin, 78(7):1028–1039, 1994.
- [35] J. Ohser and K. Schloditz. 3D Images of Materials Structures: Processing and Analysis.
20 J. Wiley & Sons, Weinheim, 2009.
- [36] M. Neumann, O. Furat, D. Hlushkou, U. Tallarek, L. Holzer, and V. Schmidt. On microstructure-property relationships derived by virtual materials testing with an emphasis on effective conductivity. In M. Baum, G. Brenner, J. Grabowski, T. Hanschke, S. Hartmann, and A. Schöbel, editors, Simulation Science: First International
25 Workshop, SimScience 2017, Göttingen, Germany, April 27-28, 2017, Revised Selected Papers, pages 145–158. Springer, Communications in Computer and Information Science (CIS), Berlin, 2018.
- [37] D. Jeulin and A. Le Coënt. Morphological modeling of random composites. In K. Z. Markov, editor, Proceedings of the CMDS8 Conference (Varna, 11-16 June 1995), pages
30 199–206. World Scientific, Singapore, 1996.
- [38] D. Jeulin. Spatial statistics and micromechanics of materials. In K. Mecke and D. Stoyan, editors, Morphology of Condensed Matter, pages 3–36. Springer, Berlin, 2002.
- [39] O. M. Pecho, O. Stenzel, P. Gasser, M. Neumann, V. Schmidt, T. Hocker, R. J. Flatt,
35 and L. Holzer. 3D microstructure effects in Ni-YSZ anodes: Prediction of effective

transport properties and optimization of redox-stability. Materials, 8(9):5554–5585, 2015.

- [40] F. Willot, B. Abdallah, and Y.-P. Pellegrini. Fourier-based schemes with modified green operator for computing the electrical response of heterogeneous media with accurate local fields. International Journal for Numerical Methods in Engineering, 98(7):518–533, 2014.

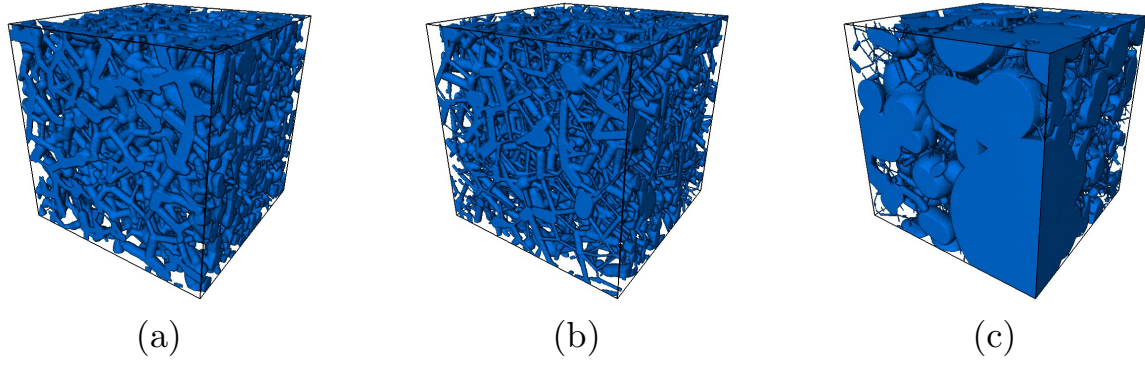


Figure 1: Visualization of virtual microstructures generated by the stochastic graph-based model. The transport phase is represented in blue. The corresponding microstructure characteristics are $\varepsilon = 0.31, \beta = 0.48, \tau = 1.40$ (a), $\varepsilon = 0.21, \beta = 0.29, \tau = 2.12$ (b), and $\varepsilon = 0.51, \beta = 0.01, \tau = 1.27$ (c).

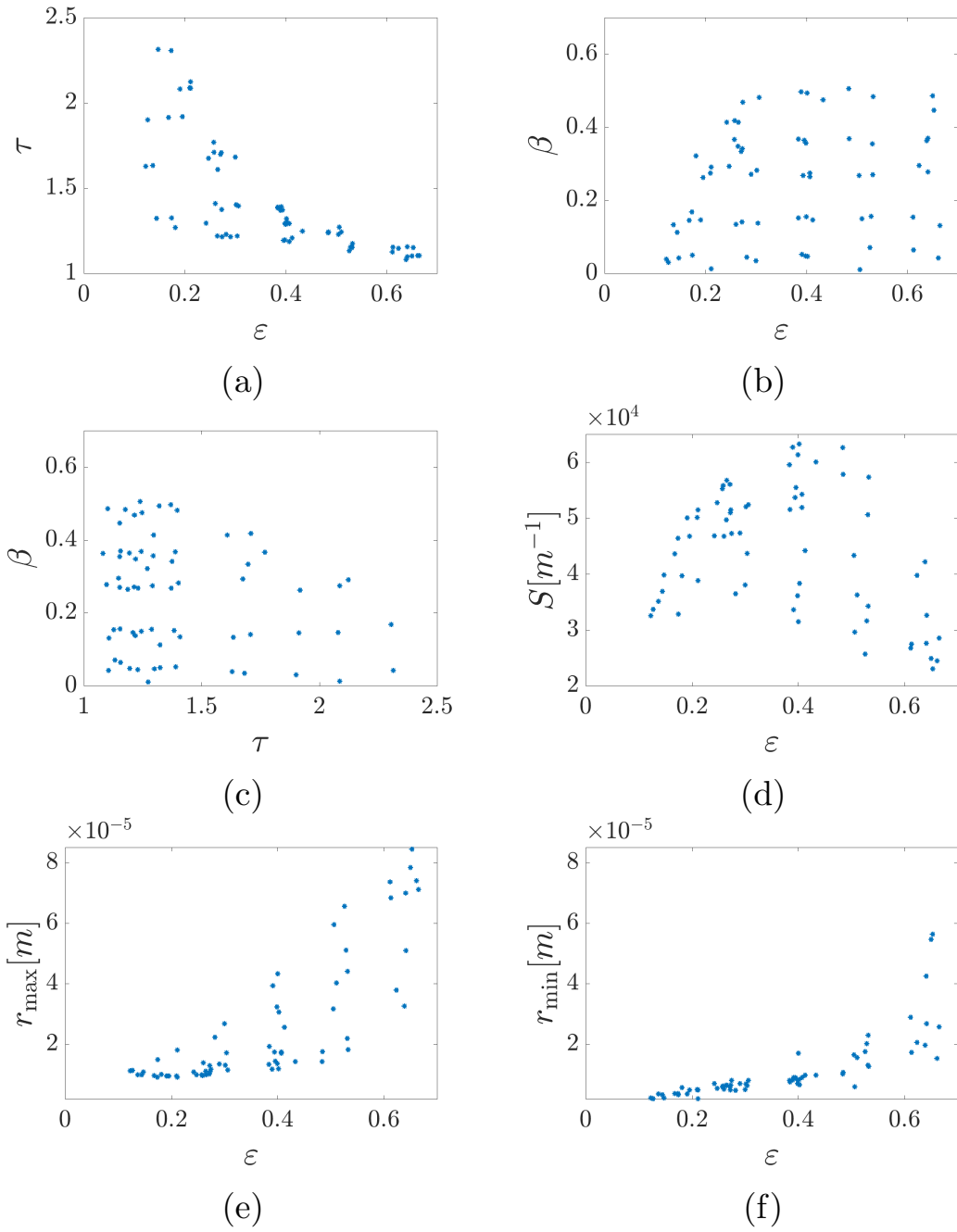


Figure 2: Microstructure characteristics of the 66 virtual microstructures considered to investigate the influence of microstructure on permeability.

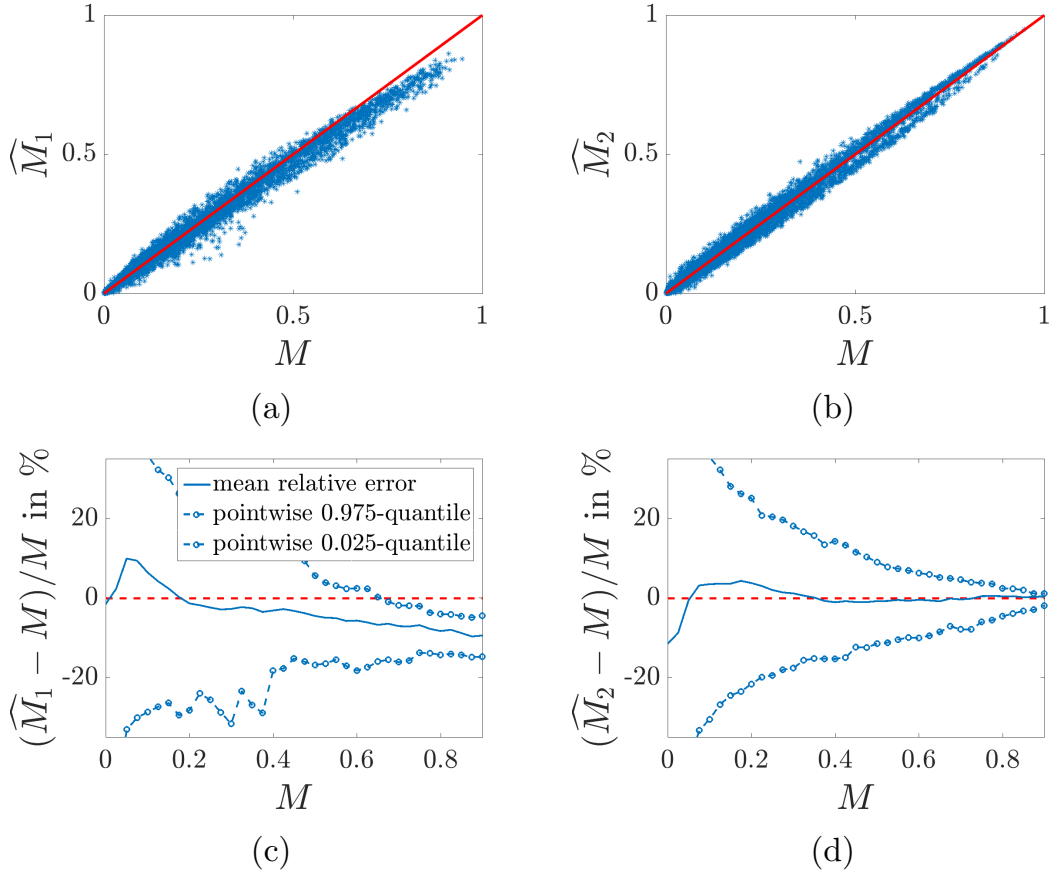


Figure 3: Top row: comparison of geometrically predicted and numerically simulated M -factor using the prediction formula presented in [17] (a) and the refined prediction formula (b), see Equations (4) and (10). Bottom row: mean of the relative error $(\widehat{M}_i - M)/M$ for $i = 1$ (c) and $i = 2$ (d) and the corresponding 0.975- and 0.025-quantiles over the M -factor, i.e., the maximum relative error of 95% of the considered virtual structures.

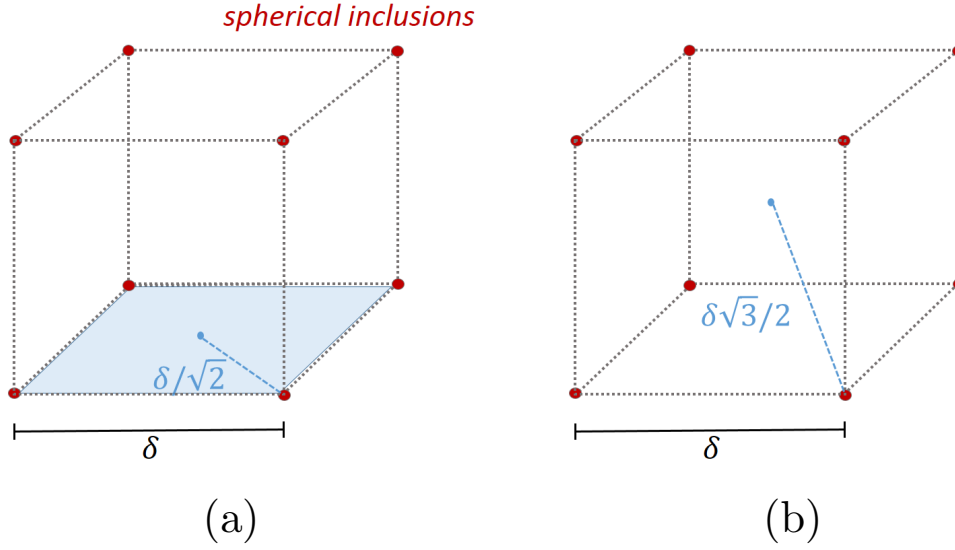


Figure 4: Conduction obstructed by non-conductive spherical inclusions (red) located on the cubic grid $\delta\mathbb{Z}^3$. Only spheres with a radius smaller than $\delta/\sqrt{2}$ can move through the structure (a), while the conducting phase can be covered by a union of spheres with radius $\delta\sqrt{3}/2$ such that these spheres are contained within the conducting phase (b).

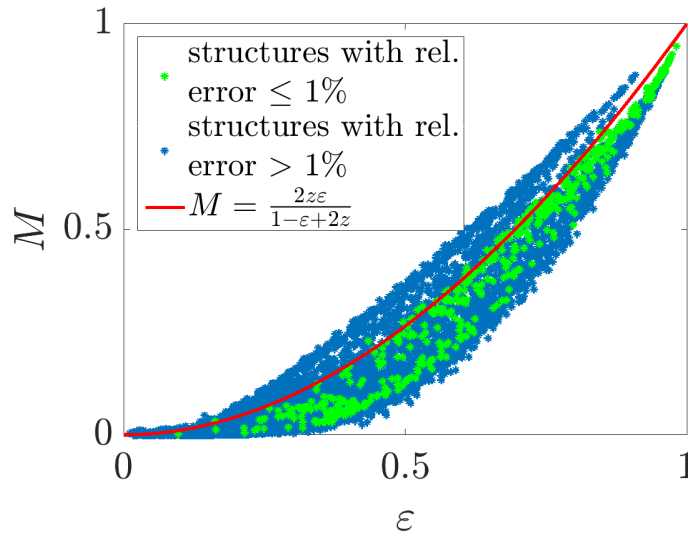


Figure 5: Relationship between ε and M for those virtual microstructures the M -factor of which is predicted with a relative error of less than 1 % by Equation (10)(green). For comparison, the results of the remaining microstructures are also included in the plot (blue). Furthermore, the theoretical upper bound for M in case of the Boolean model is drawn in red.

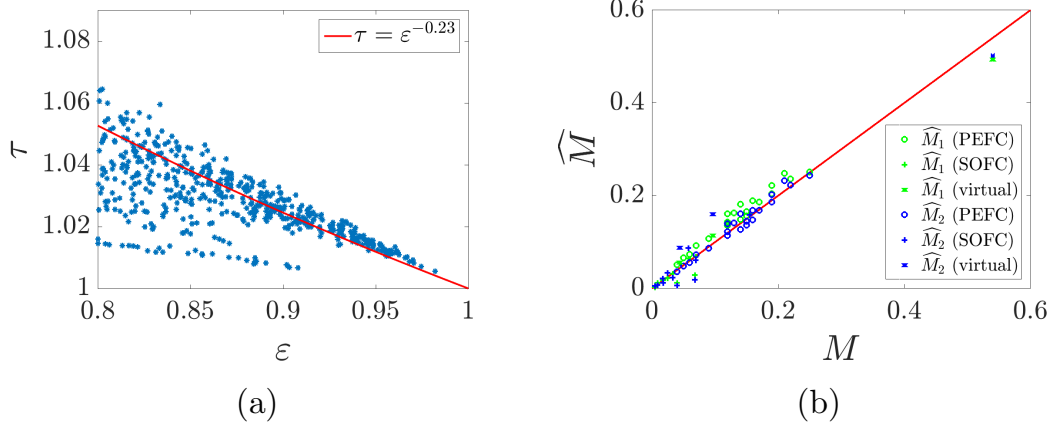


Figure 6: Mean geodesic tortuosity τ over volume fraction ε for those virtual microstructures of the 8119 ones, which have values of ε close to 1 (a) and comparison of predicted and computed properties for experimental image data representing “SOFC” and “PEFC” microstructures (b). Additionally, we show the results regarding the three virtual microstructures, which have a completely different morphology than the ones used for model fitting (b).

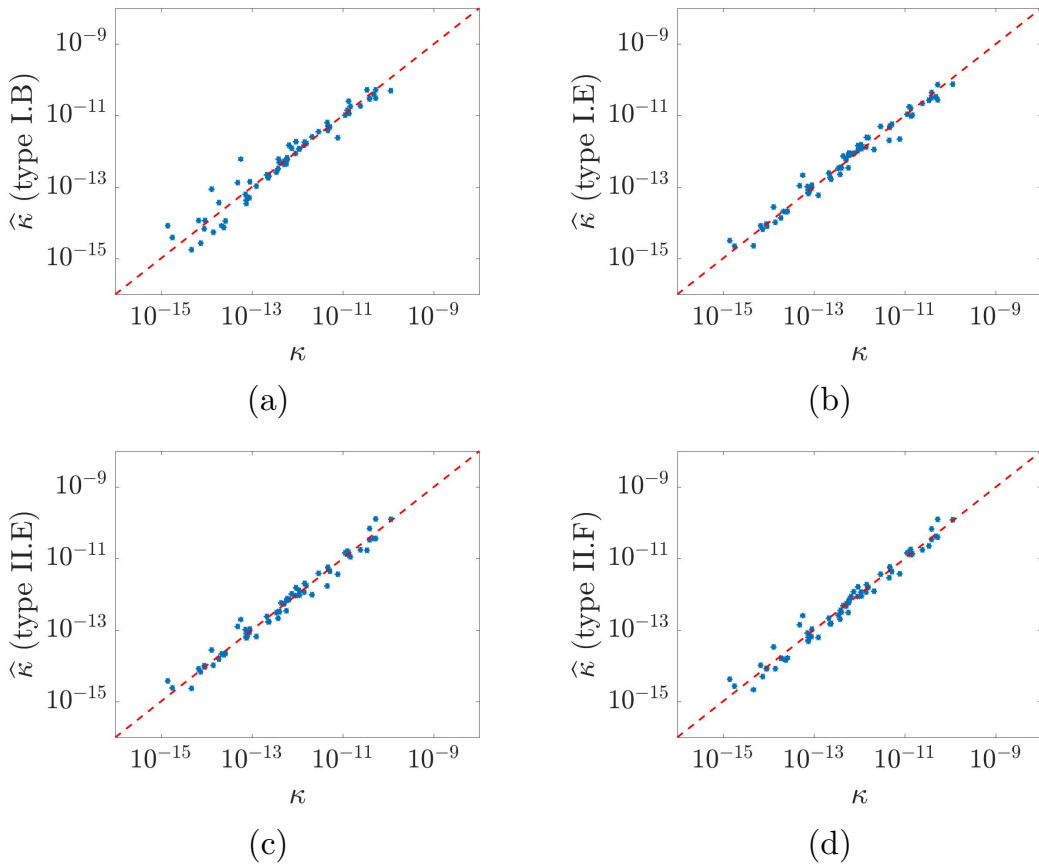


Figure 7: Comparison of geometrically predicted and numerically simulated values for permeability, where the model types I.B (a), I.E (b), II.E. (c) and II.F (d) are used for the prediction of κ .

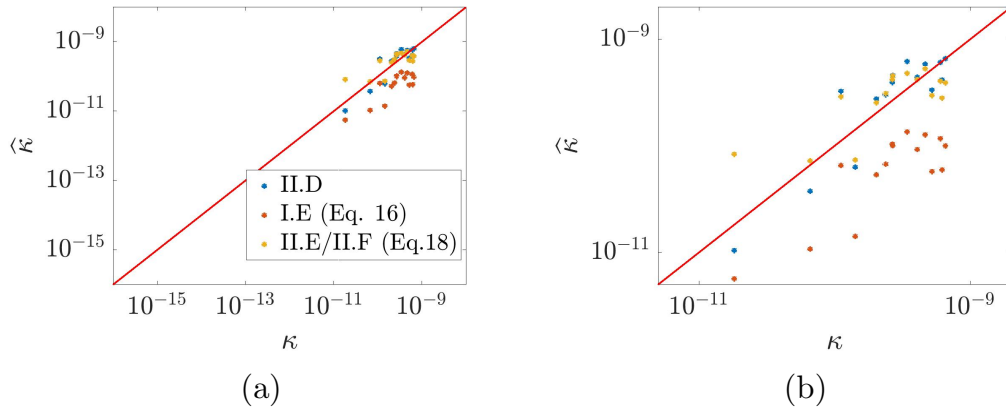


Figure 8: Comparison of geometrically predicted and numerically simulated permeability for tomographic image data representing the pore space in sponge-like structures, where predictions are performed by model type II.D, I.E and Equation (17) resulting from model types II.E and II.F (a). Zooming in the cloud of data points (b).